Applied Materials Today 35 (2023) 101926

Contents lists available at ScienceDirect

Applied Materials Today

journal homepage: www.elsevier.com/locate/apmt

Revealing the influence of edge states on the electronic properties of $PtSe_2$

Kuanysh Zhussupbekov [a,b,c,1], Lida Ansari [d,1], Kenan Elibol [e], Ainur Zhussupbekova [a,b], Jani Kotakoski [f], Igor V. Shvets [a,g], Georg S. Duesberg [h], Paul K. Hurley [d,g], Niall McEvoy [b,g,*], Cormac Ó Coileáin [b,g,h,*], Farzan Gity [d,g,**]

[a] School of Physics, Trinity College Dublin, Dublin 2, D02 PN40, Ireland
[b] School of Chemistry, Trinity College Dublin, Dublin 2, D02 PN40, Ireland
[c] Kh. Dosmukhamedov Atyrau University, Studenchesky Ave.,1, Atyrau, Kazakhstan
[d] Nanoelectronic Materials and Devices, Tyndall National Institute, University College Cork, Cork, Ireland
[e] Max Planck Institute for Solid State Research, Stuttgart 70569, Germany
[f] Faculty of Physics, University of Vienna, Boltzmanngasse 5, Vienna A-1090, Austria
[g] AMBER Centre, CRANN Institute, Trinity College Dublin, Dublin 2, D02 PN40, Ireland
[h] Institute of Physics (EIT2) & Centre for Integrated Sensors (SENS), University of the Bundeswehr Munich, Neubiberg 85579, Germany

ARTICLE INFO

Keywords:
Transition metal dichalcogenides
$PtSe_2$
Edge states
STM/STS
DFT
NEGF
Surface Green's function

ABSTRACT

The properties and performance of 2D nanostructures are known to be critically affected by localized edge states. Here, platinum diselenide ($PtSe_2$) films, synthesized by thermally assisted conversion, are characterized by a variety of spectroscopic and microscopic methods, including scanning tunneling microscopy and spectroscopy, and scanning transmission electron microscopy. We report the presence of distinct edge states, and use surface Green's function methodology in atomistic modeling of different edge atomic structures, together with other theoretical tools, to investigate their origin. Our results indicate that the edges, inherent and abundant in polycrystalline films, can be semiconducting or semimetallic in nature depending on the edge configuration. Experimental results in conjunction with first-principles calculations demonstrate a mapped band profile of the atomically-sharp step edges of $PtSe_2$, which form lateral heterojunctions possessing large asymmetric band offsets in the conduction and valence bands. We further explore the viability of a single step monomaterial heterojunction based field-effect transistor, through atomistic quantum transport simulations. This reveals the critical role of the edge states in creating a wider energy band for carrier transport in the ON-state and hence enabling a remarkably large I_{ON}/I_{OFF} ratio $> 10^{10}$ and near-ideal subthreshold slope, fulfilling the requirements for low-power applications.

1. Introduction

Owing to their wealth of unique and interesting properties, the value and potential of two-dimensional (2D) layered materials are undisputedly recognized. 2D materials evidently have the potential to revolutionize the fields of electronics, energy, and catalysis [1–7]. Critically, their exceptional properties are often not apparent in the bulk forms of the base materials. As such, methods that can produce 2D materials with controllable well-defined qualities and dimensions are essential. The morphologies of 2D materials are highly dependent on the synthesis processes and conditions. High-quality materials can be obtained by mechanical exfoliation of bulk crystals and molecular beam epitaxy (MBE), but these methods are not generally regarded as being scalable. Chemical vapor deposition (CVD) is an established route for the production of large-area, high quality films down to monolayer thickness; however, it often requires high temperatures. Other approaches such as liquid phase exfoliation (LPE) and thermally assisted conversion (TAC) can be expedient, due to their simplicity and in many cases lower thermal budget. Furthermore, the polycrystalline films produced by these methods can be highly advantageous for applications that rely on edge sites, such as catalysis and sensing [8,9]. However, understanding and characterizing the electronic features of polycrystalline films is

* Corresponding authors at: School of Chemistry, Trinity College Dublin, Dublin 2, D02 PN40, Ireland.
** Corresponding author.
E-mail addresses: nmcevoy@tcd.ie (N. McEvoy), ocoilecl@tcd.ie (C. Ó Coileáin), farzan.gity@tyndall.ie (F. Gity).
[1] Both authors contributed equally to this work.

https://doi.org/10.1016/j.apmt.2023.101926
Received 22 June 2023; Received in revised form 11 August 2023; Accepted 6 September 2023
Available online 22 September 2023
2352-9407/© 2023 The Authors. Published by Elsevier Ltd. This is an open access article under the CC BY license (http://creativecommons.org/licenses/by/4.0/).

more challenging than simple idealized structures.

As 2D materials are adopted for use and move to the forefront of materials science research, it has never been more important to understand the nature of inherent defects that modify their intrinsic properties. Due to the dimensional confinement, defects proportionally play a significant role in the electronic and atomic structure of 2D materials [10,11]. Indeed, the extraordinary responsiveness of sensors based on 2D materials can be attributed to the appreciable influence even single defects and adsorbed molecules can have [12,13]. Numerous studies have investigated the presence and influence of point defects (0D) in transition metal dichalcogenides (TMDs) [14–17]. However, for sheets with restricted lateral dimensions, 1D defects in the form of crystal edges may be the dominant defect type present. The edges of 2D materials can feature a variety of termination states including dangling bonds and edge reconstruction. These can have properties distinct from those of the 2D planes, give rise to new phenomena, and introduce additional functionalities [18–22]. It is notable that the fabrication of flexible and portable electronics and energy-storage devices by methods such as direct-ink writing of functional materials characteristically employ polycrystalline liquid exfoliated materials [23,24], whose edge states have been observed to host distinct properties [25,26]. Understanding the influence of edges becomes more critical as the thickness of the crystallites within films is reduced, as this is typically correlated with the lateral dimensions [27,28].

Since their initial identification, group-6 TMDs have been the dominant 2D semiconducting materials of choice. However, more recently group-10 TMDs, also referred to as noble-metal TMDs (NTMDs), have come to prominence due to their suitability for future nano-electronics. While the extensively studied group-6 TMDs (e.g., MoS_2, $MoSe_2$) commonly adopt the 2H phase, the NTMDs (e.g., PtS_2, PdS_2) distinguish themselves with a broader variety orderings, for example the 1T phase is typically observed for $PtSe_2$, as shown in Fig. 1(a), and PdS_2 adopts the 2O phase [29]. A member of the NTMDs that has lately drawn considerable interest is $PtSe_2$, which displays a wealth of interesting properties [30,31]. In its bulk-like state, $PtSe_2$ exhibits semi-metallic behavior, but its electronic structure can be modulated by controlling the layer number. It was predicted and confirmed to undergo a semimetal-to-semiconductor transition with reduced layer numbers [32–34]. Single- and few-layer $PtSe_2$ are typically, though not exclusively, observed to be *p*-type semiconductors with a tunable bandgap [4, 32]. It has been predicted that monolayer $PtSe_2$ undergoes an indirect-bandgap to a direct-bandgap semiconductor transition for a

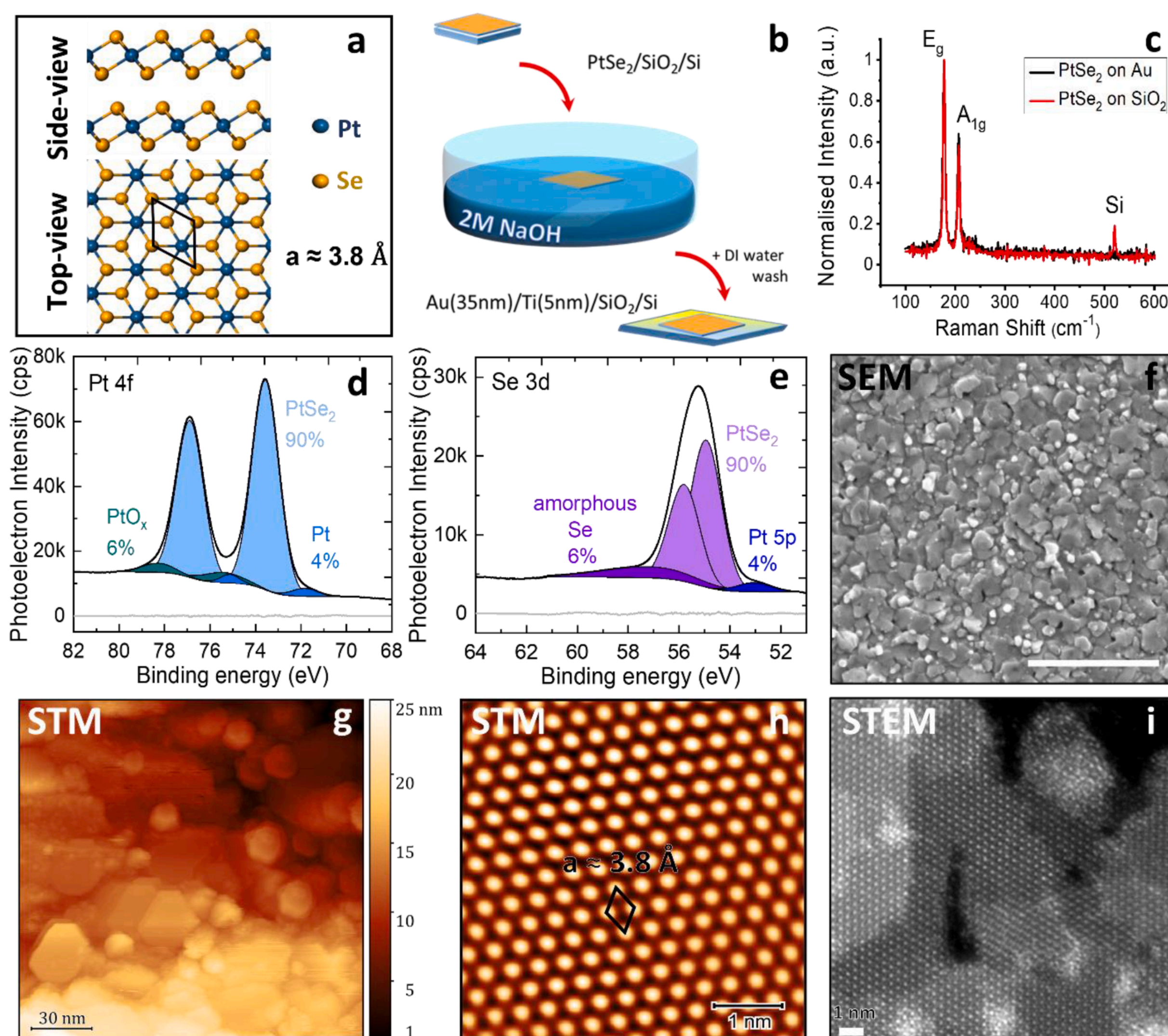

Fig. 1. Polycrystalline $PtSe_2$ films. (a) Schematic view of 1T-$PtSe_2$ crystal structure. (b) Schematic of the lift-off and transfer process. (c) Raman spectra of $PtSe_2$ film before and after transfer, showing characteristic $PtSe_2$ peaks and an additional Si peak at 520 cm^{-1} from the original substrate. XPS of $PtSe_2$ film showing the Pt 4f (d) and Se 3d (e) core levels. (f) SEM image of transferred $PtSe_2$ film (scale bar is 500 nm). (g) STM image of a $PtSe_2$ film displaying crystals (170 × 170 nm, V = 1.2 V and I = 34 pA). (h) Atomic-resolution STM image in a defect-free area with an interatomic distance of 3.8 Å (5 × 5 nm^2, V = 0.2 V, I = 650 pA). (i) HAADF-STEM image of multilayer 1T-$PtSe_2$ (scale bar is 1 nm).

strain of 8% [35]. Notably it exhibits high charge-carrier mobility, with experimental values ranging to ~625 $cm^2 V^{-1} s^{-1}$, [36] and a theoretical mobility comparable to that of black phosphorus, [37,38] but with the benefit of much greater in-air stability. These remarkable semiconducting properties come in conjunction with other notable electronic properties. Studies have suggested its suitability for electrically-tunable spintronic applications, [39,40] and with strain playing an important role in its performance, $PtSe_2$ is proposed to have one of the highest Seebeck coefficients among the TMDs [41,42]. In addition, the relatively low synthesis temperature of $PtSe_2$ by TAC enables back-end-of-line (BEOL) integration and the growth of the material directly on polymer substrates for strain gauges [43,44]. In light of these beneficial properties, $PtSe_2$ has demonstrated potential for application in areas such as transistor electronics, [32,45,46] broad spectrum photo-detection [47, 48], catalysis [8,49,50], and gas sensing [31]. Quality is an important factor, it has been reported that defects can induce magnetic ordering in $PtSe_2$ [10,51]. Furthermore, variations of crystallite size in polycrystalline films have been reported to influence the $PtSe_2$ film properties, e.g. mobility, suggesting edge density might also be a contributing factor [52]. Indeed, specifically related to crystal edges, it has been shown that the density of edge sites can be controlled during synthesis [8], which could be beneficial for catalysing the hydrogen evolution reaction [53].

The properties of crystal edges are widely relevant to 2D materials, moreover, $PtSe_2$ presents an inherently interesting system to study such edge effects. It has been suggested that energy profiles at the step edges is qualitatively different depending on the strength of the interlayer interaction, which is a consideration for materials with stronger interlayer interactions such as $PtSe_2$ [19]. From an application viewpoint, self-contacting devices are possible due to the semimetal-to-semiconductor transition with reduced thickness, and such geometries will necessarily possess such edges [54]. Furthermore, it is anticipated that the strong quantum confinement effect in $PtSe_2$ results in a rather large band offset in the conduction band and/or valence band due to the thickness variation at the edge, creating a monomaterial heterojunction. Vertical stacking of layered materials to create heterojunctions is a subject of ongoing research, but given the challenges associated with the growth of the dissimilar materials, monomaterial heterojunctions with atomically-sharp interfaces and uniform chemical composition offer an opportunity to engineer more ideal Schottky barriers and novel device concepts for nanoscale field-effect transistors (FETs) [55–57].

Step edges are a dominant feature within polycrystalline films, therefore insights into the electronic states such features are valuable for the application of such films in devices or for catalysis, and also ultimately for self-contacting architectures. Using complementary techniques, here we investigate and discuss the electronic nature of the step edges on $PtSe_2$. Polycrystalline $PtSe_2$ is a practical system that offers plentiful step and edge features to experimentally examine. Low-temperature scanning tunneling microscopy (STM) and scanning transmission electron microscopy (STEM) provide atomic-resolution images of the crystallites within the polycrystalline films, while scanning tunneling spectroscopy (STS) is used to map the local density of states (LDoS). High-angle annular dark-field (HAADF) STEM imaging is used for elemental identification of isolated atoms in crystallites, through its Z-contrast property, which enables understanding of the edge terminations of $PtSe_2$ crystals. In order to understand the band alignment and explore the possible applications of the monomaterial heterojunction, we systematically study the electronic properties of different edge terminations in monolayer (ML) and bilayer (BL) $PtSe_2$ separately, in addition to those in a ML-BL $PtSe_2$ heterojunction, using first-principles calculations.

2. Results

$PtSe_2$ was synthesized through the TAC of Pt films [31]. Pt thin films, with thicknesses up to 5 nm, were deposited on SiO_2/Si substrates by argon-ion sputtering. The 1T atomic structure of the $PtSe_2$ is shown in Fig. 1(a). $PtSe_2$ was obtained by annealing the samples at 450 °C for two hours under a 150 sccm H_2/Ar flow in the presence of an upstream-heated elemental Se source. As a conductive substrate is required for electrical measurements, e.g. STM/STS, the $PtSe_2$ films were liberated from their insulating growth substrates by etching in 2 M NaOH solution and floated onto Au/Ti (30 nm/5 nm) on SiO_2/Si substrates, as illustrated in Fig. 1(b) and further described in the experimental section. The conversion process yields matted polycrystalline films, and the morphology at each stage, before and after transfer, was verified by atomic force microscopy (AFM), Fig. SI1. Raman spectroscopy and X-ray photoemission spectroscopy (XPS), Fig. 1(c–e), were used to assess and confirm the synthesis of the $PtSe_2$ films. Raman spectra of as-grown and transferred films, shown in Fig. 1(c), display the characteristic E_g and A_{1g} modes verifying the successful synthesis and transfer of $PtSe_2$ [58]. XPS was conducted to investigate the compositional quality of the $PtSe_2$ films. All energy positions were corrected with respect to the adventitious carbon peak at 284.8 eV. Fig. 1(d, e) demonstrate the spectra of the Pt 4f and Se 3d core-level regions of a representative film (5 nm thick starting Pt film) of $PtSe_2$. The Pt 4f core-level spectrum is deconvoluted into three contributions: the main doublet peak at ~ 73.5 eV (4f 7/2) which is attributed to $PtSe_2$; the smaller peaks positioned at ~ 75.4 eV and 71.8 eV which can be ascribed to Pt-oxides and unreacted Pt metal, respectively [31]. XPS shows that about 6% amorphous Se, likely due to the excess required for the TAC process. The majority of the Pt is bound to Se, however some oxides and elemental Pt persist. This is consistent with previous XPS studies of $PtSe_2$ produced by this method [31]. The Se 3d core-level spectrum is composed of two contributions: the dominant one from $PtSe_2$ at 54.9 eV and the other relatively small one positioned at higher binding energy of 55.8 eV possibly indicative of the amorphous Se [59]. The atomic percentage of Pt and Se in the film contributing to $PtSe_2$ is determined to be approximately 34.7% and 65.3%, respectively.

STM was used to study the morphology and crystal structure of the polycrystalline TAC-grown $PtSe_2$ films, which revealed features comparable to those observed in other STM studies [60–62]. The large-scale features visible with scanning electron microscopy (SEM), Fig. 1(f), are also apparent in the STM images of the film, shown in Fig. 1(g). Large-area STM scans show many grains have hexagonal shapes (Figs. 1 (g) and SI2(a) & (b)). It can also be seen that there is some contamination present on the surface of the sample. The film morphology as observed by STM is consistent with the AFM measurements (Fig. SI1). The crystallinity of the $PtSe_2$ grains and the high density of steps at the crystal edges is further highlighted in Fig. SI2(b). It can be seen from the line profiles, Fig. SI2(c), that the $PtSe_2$ crystallites' thickness typically varies from 1 to 6 nm. From atomically-resolved images of the surface, such as Fig. 1(h), an average lattice constant of 0.38 nm is obtained, which matches very well with earlier reports [14,30]. It should be noted that not all sites were defect free, and the observed 0D defects, such as those shown in Fig. SI3, are consistent with another recent STM study, the contrasting synthesis approaches notwithstanding [14,63]. The STM analysis reveals a number of distinct 0D defects on the $PtSe_2$ film, e.g., at least three 0D defects identified under positive and negative bias voltages in the atomically-resolved STM images shown in Fig. SI4. From basic STM analysis it can be concluded that the films are edge rich and the polycrystalline grains can reach 40 nm in lateral size, and 0D defects are evident in some areas.

In HAADF-STEM images, Figs. 1(i) and SI5(a), multilayers with different edge terminations are apparent. HAADF imaging, which is also called Z-contrast imaging, not only allows dynamics and positions of atoms to be monitored but also enables elements to be identified since the HAADF signal increases with the atomic number Z as $Z^{1.64}$ for isolated atoms (the intensity of signal changes almost linearly with the sample thickness) [64]. The termination of edges and the number of $PtSe_2$ layers can therefore be identified from the HAADF signal intensity.

The brightest atoms on the images correspond to the Pt ($Z = 78$) whereas less bright atoms are Se ($Z = 34$). It should be noted that HAADF is not a spectroscopy mode and the elemental identification of heteroatoms is not possible if the atomic numbers of heteroatoms are close or the specimen imaged is of unknown composition. As the intensity changes linearly with thickness, the number of $PtSe_2$ layers varies between 1 and 5 in Fig. 1(i) (see also Fig. SI5(b)).

Atomic resolution HAADF-STEM images of monolayer $PtSe_2$ with two different terminations and the corresponding density functional theory (DFT) relaxed atomistic models are shown in Fig. 2(a–d). Since the edge atoms have fewer neighbors compared to atoms at the smooth surfaces, the atoms at the edge of TMDs are chemically more active and unstable under electron beam irradiation in STEM [65–67]. Fig. 2(a, b) shows that the Se-terminated (type A configuration) edge of ML $PtSe_2$ has more atoms compared to the Pt-terminated edge (type B configuration) as shown in the atomistic models in Fig. 2(c, d). The reconstructed type A edge configuration (Fig. 2a) therefore looks complex while the type B configuration (Fig. 2b), with fewer edge atoms, is straight and more stable. The raw HAADF images of type A and B edge configurations are shown in Fig. SI5(c, d). To gain further insight into the atomistic effects of edges in $PtSe_2$, we investigated the edge structural configurations and electronic properties of $PtSe_2$ using fully

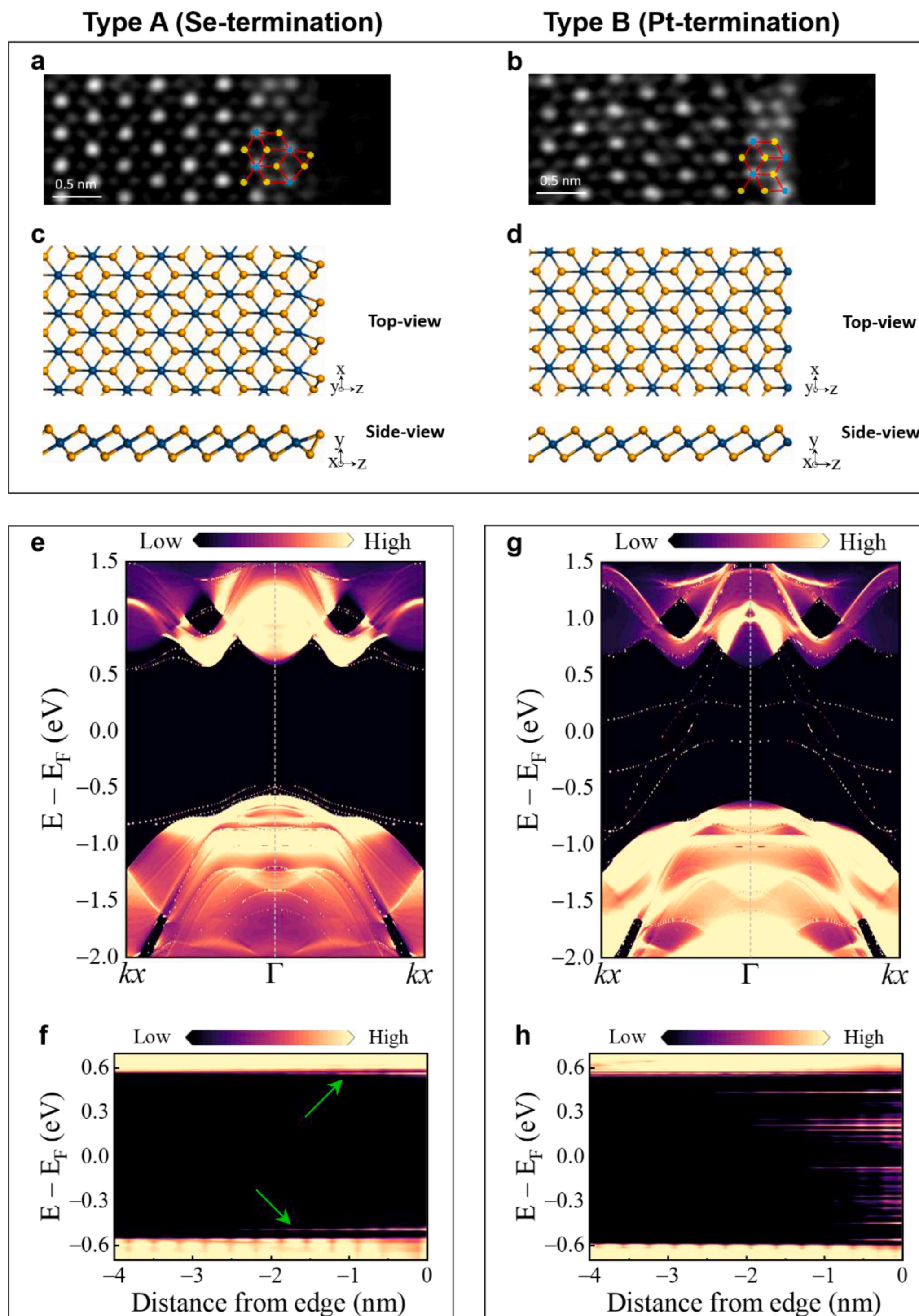

Fig. 2. Different edge configurations and their impact on the electronic structure of ML $PtSe_2$. Left: type A configuration (Se termination). Right: type B configuration (Pt termination). Filtered atomic-resolution HAADF-STEM images of ML $PtSe_2$ with Se (a), and Pt (b) terminations. Blue and yellow spheres represent Pt and Se atoms respectively in the model in (a) and (b). The raw HAADF images are shown in Fig. SI5(c,d). Atomic structure post geometry relaxation for Se terminated (c), and Pt terminated edges. (d) $PtSe_2$ viewed from side and top. (e) Contour plot illustration of the band structure projected at the edge of type A configuration, i.e. on the Se atom at the edge, considering SOC. (f) Magnified LDoS displaying the spatial extent of the edge-induced states in the bandgap in real space along the $PtSe_2$ ML layer from the edge. (g and h) Edge band structure, projected on the Pt atom at the edge, and magnified LDoS for type B edge. Energy states are created in the bandgap as a result of the edge configuration. The density of these edge-induced states and their energy distribution across the bandgap are more pronounced in type B edge configuration compared to type A (shown by green arrows in (f)).

relativistic first-principles calculations (see Experimental Methods for details). Both type A and type B edge configurations were considered for monolayer (ML) and bilayer (BL) $PtSe_2$. Shown in Fig. 2(c, d) are the side-view and top-view of the relaxed structures of ML $PtSe_2$ with Se- and Pt-terminated edge configurations. Although the edge is reconstructed in the type A termination, as can be conspicuously seen in Fig. 2 (d), no considerable reconstruction was observed in type B compared to the as-cut structures. Notably, in the type B configuration, there is a contraction of Pt-Se bond lengths ($b_{Pt\text{-}Se}$) at the edge from 2.54 Å to 2.42 Å while in type A there is a slight increase of $b_{Pt\text{-}Se}$ from 2.54 Å to 2.57 Å.

A third zigzag termination is also possible (type C). The atomic structures before and after geometry optimization are shown in Fig. SI6. As can be seen, no significant reconstruction is observed at the edge. The surface band structure including spin orbit coupling (SOC) is also included in the SI, Fig. SI8. Including SOC in calculations for this edge configuration (type C) leads to distinguishable spin splitting of the edge states, but not as pronounced as for type B edge states. It also leads to slight bandgap opening while calculations without SOC show metallic edge states. Compared to type A, although the edge states do not form a metallic edge, the edge states are distributed across a wider energy band in the bandgap; nonetheless, they do not cross and hence the edge is not metallic.

To investigate the effects of SOC on the edge states, fully relativistic pseudo potentials were used. The electronic structure of the two edge types for the ML $PtSe_2$ structure is presented in Fig. 2(e–h), demonstrating a bandgap of ~1.2 eV for monolayer $PtSe_2$, which is consistent with literature values [32,63]. A contour plot of the band structure projected on the Se atom at the edge considering SOC is shown in Fig. 2 (e). The edge-induced states are localized at energies close to the conduction band minimum and valence band maximum with spatial distribution of ~2.5 nm from the edge of the structure, as identified in the LDoS at the edge of the structure (green arrows in Fig. 2(f)). As depicted in Fig. 2(g), which demonstrates the edge-band structure projected on the Pt atom at the edge, a large density of edge-induced energy states is created throughout the bandgap at the edge of the Pt-terminated ML $PtSe_2$ both above and below the Fermi energy (E_F), closing the bandgap and making the edge metallic. Similar to type A configuration, edge states in type B also extend ~2–2.5 nm from the edge (Fig. 2(h)). Such spatially and spectrally localized edge states could contribute to percolated conduction through the $PtSe_2$ crystallite edges in a polycrystalline film and be a contributing factor to the enhanced edge conduction observed by conductive AFM (see Fig. SI9). The presence of edge states is known to similarly impact the electrical performance of MoS_2 crystals [68]

Edge band structures of types A and B edge configurations without SOC are provided in Fig. SI10. As can be seen, considering SOC breaks the degeneracy of the edge-induced states created in the bandgap. For the type A edge configuration, zero spin splitting is observed for the edge states at the Γ point while they develop a relatively small spin splitting at wavevectors away from the Γ point. For the type B edge configuration, on the other hand, the metallic edge states (shown by dashed lines in Fig. SI10(c) and labeled a and b) demonstrate significantly large splitting, i.e., the **a** and **b** energy bands split into **a'** and **a''**, and **b'** and **b''** bands when SOC is considered. Maximum splitting of the **a** band occurs at an off-Γ wavevector with the value of $\Delta E_a = 385$ meV while it reduces to 320 meV at the Γ point. The **b** band exhibits splitting with a maximum value of $\Delta E_b = 450$ meV at *kx* (*kx* represents the edge of the Brillouin zone in the *x*-direction where the $PtSe_2$ structure is periodic). Moreover, the spin magnetic moment for type-B configuration at the Pt edge site is 0.39 μ_B (Bohr magneton), which is strongly localized at the edge and diminishes quickly with distance from the step edge (450% reduction in ~0.3 nm from the edge, i.e., edge-state magnetism), while for type-A it is 0.003 μ_B. This sizable spin magnetic moment for the Pt-terminated edge is comparable to the reported values for graphene and black phosphorus [69,70]. Such large spin splitting of the energy bands and magnetic moments of the $PtSe_2$ edge structure would be very promising for spintronics applications. The edge band structure of type C configuration (single Se-termination) of ML $PtSe_2$ is shown in Fig. SI8. A bandgap of ~130 meV was determined for this type of edge when SOC was considered, which is in agreement with literature [63]

The edge band structure and LDoS of BL $PtSe_2$ is presented in Fig. SI11. This figure demonstrates that no states are created in the bandgap for the type A edge (Se-terminated) configuration, while similar to ML $PtSe_2$, but type B creates a large density of metallic states across the bandgap. The relative formation energies of the three types of edge configuration, i.e., type A (Se-terminated, stoichiometric edge), type B (Pt-terminated, non-stoichiometric edge with 2 Se atoms missing) and type C (single Se-terminated, non-stoichiometric edge with 1 Se atom missing) are shown in Fig. SI12. As can be seen, the edge formation energy is parameter dependent and our calculated energies versus the Se chemical potential are found to be consistent with the published data; i. e., the edge formation energy of the stoichiometric edge configuration (type A) is independent of the chalcogen (in our case Se) chemical potential while the nonstoichiometric edge terminations (type B and C) are dependent on the chalcogen (in our case Se) chemical potential [63,71, 72]

A more detailed experimental examination of the crystallite steps, and an investigation of their localized electronic structures, is desirable for comparison with models and for a better understanding of the film properties. Conductive AFM measurements, Fig. SI9, at a set bias revealed larger currents at the step edges, which would suggest current percolates through these pathways [68]. However, it could be argued that the improved conductivity could be attributed to better contact between the edge and tip at these points, as would be expected for an edge-contacted 2D material [27]. A more rigorous approach is to use high-resolution STS, which can provide mapped information on the density of electrons as a function of their energy. As can be seen from Fig. SI2, the crystallite with the bilayer step edge where STS was performed is at least 3 layers thick. In STS, variations in the tunneling current with voltage are due to differences in the electronic structure, and a map of the electronic structure can be built up by sweeping the bias in a systematic site-by-site manner [73,74]. An STM/STS investigation of the step edges reveals the existence of distinct edge states. Fig. 3(a) shows an STM image of a $PtSe_2$ bilayer step edge (~1.2 nm) and the grid spectroscopy measurements performed on the step within this area. 50 × 50 individual I(V) measurements were performed in a grid with dimensions of 10 × 10 nm^2 (Fig. SI13(b, c)). The voltage was swept between ±1 V. Fig. 3(b) depicts the dI/dV map at electron energy value of -0.2 V, which corresponds to the filled states. Brighter points on the grid correspond to a higher DoS at -0.2 eV. This dI/dV map is characterized by bright lines corresponding to the terrace edge of the $PtSe_2$. It is interesting to note that the step edge exhibits a higher DoS compared with the flat terraces. These altered electronic properties at the step edge resemble ripples gradually reducing in amplitude further away from the edge. This is understood in terms of edge states, which have different electronic properties from the flat surface. It can be seen that there are states on the lower terrace at certain energies (Fig. SI13(d)) which is in line with our DFT calculations for a single layer step presented in Fig. SI14. Corresponding current (I/V) maps of the occupied and empty states, taken at bias voltages of around -0.3 and 0.24 V, are shown in Fig. SI13(b, c). Fig. 3(c) displays dI/dV plots (numerical derivative of I (V)) spectra of three points indicated on the grid by the colored stars, positioned on the flat terraces below and above the step, and at the step edge. It can be seen that the LDoS increases at the edge of the step in comparison with the flat terraces. The LDoS of the filled states at the step edge is several times larger than that measured on the pristine terraces. However, the LDoS of the empty states at the step edge differs only slightly from that of the pristine terraces, except in the window from 0.16 to 0.47 V above the Fermi level where it is slightly lower [19]. From the extended dI/dV plot in the log scale in Fig. SI13(d), which also compares lower side of the step edge, it can be observed that there is no band gap but rather a reduced density of states. The spatial distribution

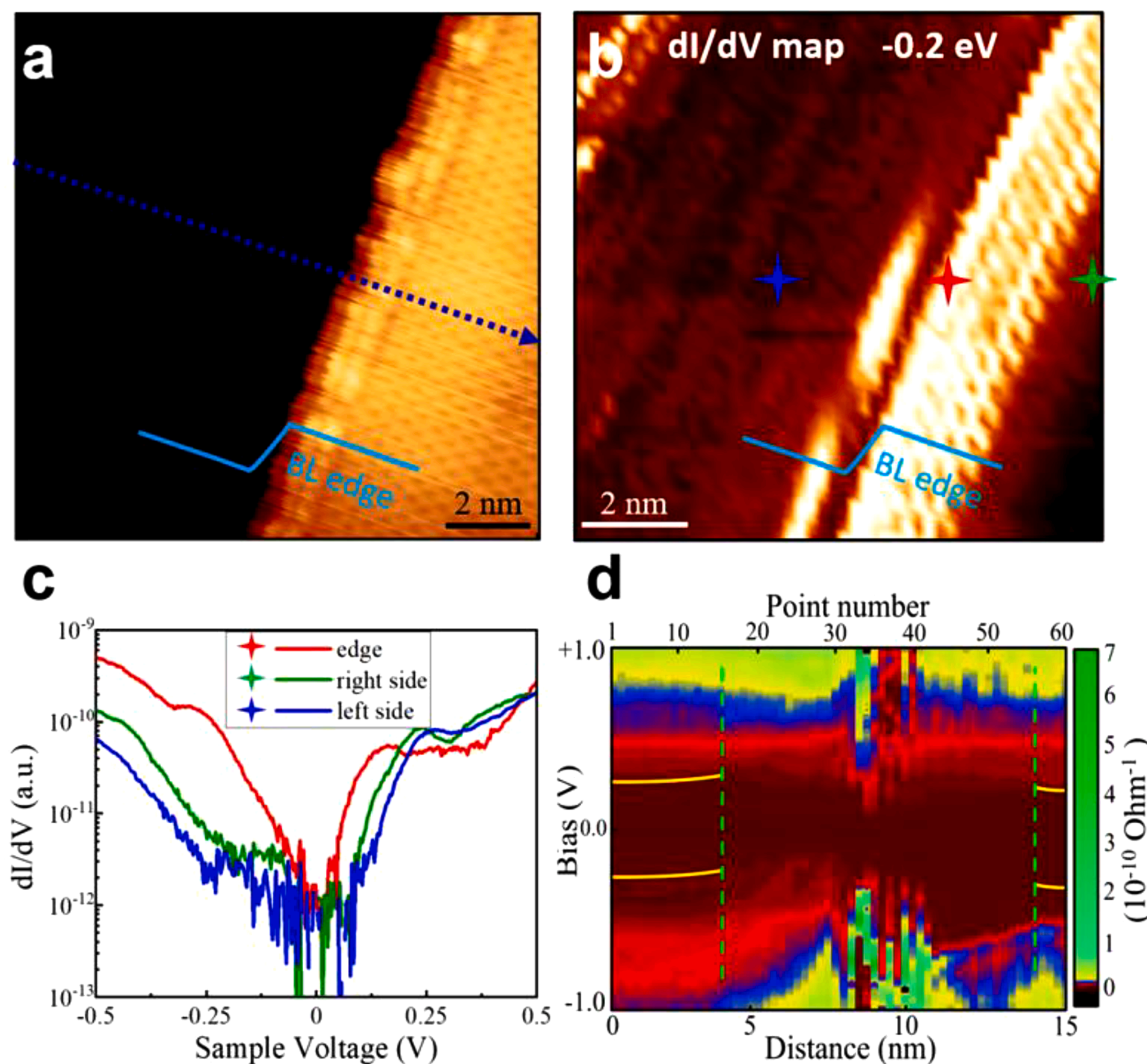

Fig. 3. Grid spectroscopy and band alignment at the edge of $PtSe_2$. (a) STM topography of bilayer step edge on multilayer $PtSe_2$ crystallite (13 × 13 nm^2, V = 0.8 V and I = 100 pA). Grid spectroscopy (10 × 10 nm^2) was performed within the area in (a). (b) Grid dI/dV mapping (50 × 50 points) at electron energy value of -0.2 eV. Bright lines (higher DoS) correspond to the edge states of $PtSe_2$ terrace exhibiting ripples gradually reducing in amplitude further away from the edge (stabilization parameters V = 0.8 V and I = 100 pA). (c) Representative dI/dV spectra of three points in the grid indicated by the colored stars (blue, green and red) in (b). (d) 2D plot of tunneling spectra (dI/dV in bias range ±1.0 V) across the blue dashed arrow in (a), demonstrating an increase of the LDoS on the edge of the bilayer $PtSe_2$ step. The lines are included to illustrate the trend.

of the edge states was obtained by dI/dV mapping. Fig. SI13(e–h) correspond to the dI/dV mapping at electron energies E= -0.4, -0.2, 0.2 and 0.4 eV, respectively. Note that since the imaged areas are more than 3 layers of $PtSe_2$ there is no band gap, which is in agreement with other recent studies [33,63]. Therefore, here the apparent band bending corresponds to the localized transition between low and high DoS. To provide insight into this observation, we constructed an atomistic model of a bilayer-monolayer (BL-ML) $PtSe_2$ structure with a Pt-terminated edge. A Pt-terminated edge was considered since it was expected to generate a large DoS localized at the edge (see Fig. 2(g and h)), consistent with our additional observation of high conductivity at the flake edges (see Fig. SI9(b)). Although the experimental measurements are for a thicker bulk-like semimetallic structure and the calculated BL-ML structure is semiconducting, both compare favorably and demonstrate the presence of edge states. In other words, the features associated with the 'transition region' at the step-edge are broadly consistent for both the experimental (Fig. 3(d)) and the simulated (Fig. SI14(a)) results. Moreover, the overall trend of the band bending (Fig. 3(d)), which would be attributed to the localized transition between low and high DoS at regions away from the step-edge, is in good agreement with the simulation results (Fig. SI14(b)). The projected density of states (PDoS) at the BL-ML junction obtained within the framework of DFT and non-equilibrium Green's functions (DFT+NEGF), see Experimental Methods for details, is presented in Fig. SI14(a) for energies above the Fermi level. Each ribbon illustrates the atom-resolved PDoS at individual layers over a distance of ~1.65 nm at either side of the edge. The inset shows PDoS at a given energy of $E - E_F = 0.53$ eV which demonstrates similar ripples in the DoS to those measured experimentally. A similar characteristic is also observed at energies in the valence band (see Fig. SI14(c)).

The band profile of the $PtSe_2$ across the step edge was measured by line STS. Spectra were measured every 0.25 nm along the blue dashed arrow (15 nm) in Fig. 3(a). The resulting dI/dV data is plotted in Fig. 3 (d) as a 2D map [75,76]. Each vertical band charts dI/dV between -1.0 V and +1.0 V of a point along the line, with the magnitude of dI/dV expressed using a color intensity scale. The 2D map shows the evolution

of the edge states on this line. It should be noted that the line- and grid-STS measurements were performed on the atomically resolved and defect-free step (see Fig. 3(a)). An increase of the LDoS near the Fermi level is observed at the bilayer step edge. Although these experimental measurements are for a ~1.1 nm step, corresponding to a bilayer, and on a semimetallic film a few nanometers thick, a similar trend in band bending was obtained for the BL-ML heterojunction simulations despite these fundamental differences, as shown in Fig. SI14(b). This would appear to suggest that such features at step edges are an intrinsic feature for $PtSe_2$ even for non-ideal conditions as represented by a polycrystalline film. The upward conduction and valence band bending at both sides of the edge adjacent to the interface is also consistent with previous reports [19,75]. Notably, a localized potential barrier in the conduction band is formed at the BL-ML interface which is expected to play a crucial role in carrier transport across the heterojunction. Moreover, a ~2.5 nm transition region can be identified, shown by the vertical dashed lines (see Fig. SI14(b)). Fig. SI15 also demonstrates a rather large valence band offset ($DE_V \approx 0.8$ eV) at the BL-ML interface which is considerably larger than the conduction band counterpart. Asymmetric band offsets have also been reported for ML-BL $MoSe_2$; [75]. however, the much larger band offsets observed in the ML-BL $PtSe_2$ could be attributed to the stronger interlayer interaction in $PtSe_2$ [32]

To investigate the properties of the monomaterial BL-ML heterojunction for potential applications in the next generation of FETs, the BL-ML edge region was considered as the channel of a back-gated FET. Performance of the BL-ML monomaterial heterojunction is compared with that of a uniformly-thick ML structure as a reference back-gated FET device. A detailed description is provided in the Experimental Methods. The atomic structure of the back-gated devices is illustrated in Fig. 4(a).

To obtain the back-gated FET transfer characteristic, the gate-source bias (V_{GS}) is swept at a given drain-source bias (V_{DS}) – see Experimental Methods for further details. The I_{DS}-V_{GS} characteristic at $V_{DS} = 0.2$ V and at different V_{GS} values for both the BL-ML heterojunction and the reference ML device are shown in Fig. 4(b). Both devices demonstrate large ON/OFF current ratios, with nearly 3 orders of magnitude enhancement for the BL-ML device. The ML device demonstrates a subthreshold slope of 102.5 mV/decade, while the BL-ML device exhibits a remarkably low subthreshold slope of 64.3 mV/decade which is very close to the 60 mV/decade limit required for low-power applications.

The impact of the gate field on the band alignment at the BL-ML interface, illustrated in Fig. 4(c) in the ON-state ($V_{GS} = 0.3$ V), is expected to play an important role in the current conduction. The gate electrode itself shifts the energies to lower levels compared to a structure with no gate - see Fig. SI16. Applying a positive gate field further shifts the energies to lower levels leading to the total collapse of the band offset at the BL-ML interface, causing the conduction band edge of the ML-side to align with the conduction band edge of the BL-side of the junction in the gated region. This coupling of the conduction band states at the BL and ML sides, which could be strengthened by the edge states, creates a transport path for electrons, as depicted by the energy-resolved current in the ON-state in Fig. 4(d). However, this is not the case for the ML device, where the ML bandgap blocks the carrier transport for energies just below source chemical potential, limiting the carrier transport path (see magnified plots in Fig. SI17). As a result, and by comparing LDoS and energy-resolved current plots of the ML and BL-ML devices in the ON-state in Fig. SI17, the effective energy window between the source and drain chemical potentials ($V_{DS} = 0.2$ V), through which electrons can flow, is wider for the BL-ML structure (DE = 330 meV) than the ML structure (DE = 220 meV). This leads to the ~3 times larger ON-state current of the BL-ML structure compared to the ML device observed in the transfer characteristic in Fig. 4(b).

The LDoS and energy-resolved current of the BL-ML structure in the OFF-state ($V_{GS} = -0.6$ V), presented in Fig. 4(e, f), reveal that the carrier transport mechanism in this state is due to the tunneling through the ML region, i.e., the tunneling length is equal to the length of the ML side of the channel. Hence, to allow a fair comparison between the performance of the two device architectures, the tunneling length of the uniformly-thick ML device was set to equal the tunneling length of the BL-ML

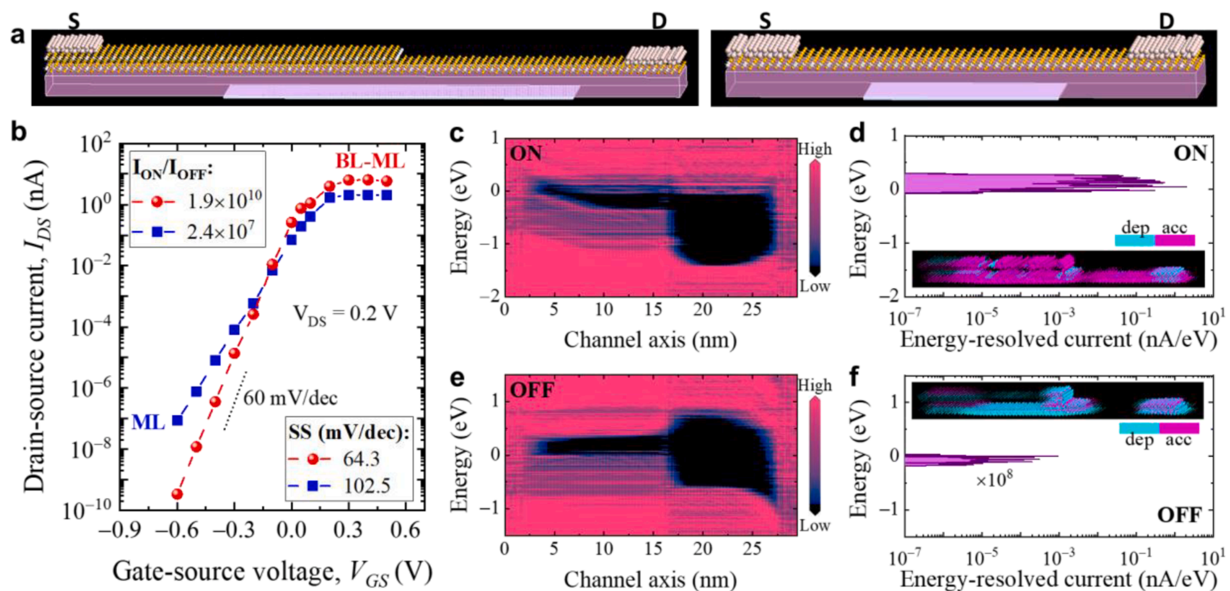

Fig. 4. Back-gated field effect transistors (FETs) and their properties. (a) Atomic structure of FET devices with BL-ML $PtSe_2$ (left) and uniformly-thick ML $PtSe_2$ (right) as device channel. (b) Transfer characteristic of the simulated devices, comparing the performance of the BL-ML FET of the edge, with ML FET, at $V_{DS} = 0.2$ V. BL-ML device demonstrates $> 10^{10}$ I_{ON}/I_{OFF} ratio, with subthreshold slope (SS) of just above the 60 mV/decade limit. Notably, the ML device exhibits more than 2 orders of magnitude larger OFF current compared to the BL-ML FETs. (c) LDoS of the BL-ML device at the ON bias condition revealing the impact of the gate field on collapsing the potential barrier at the BL-ML interface leading to the large ON current. (d) Energy-resolved current of the BL-ML device at the ON bias condition demonstrating the effective energy states contributing to the carrier transport from the source to drain in the ON-state. (e) LDoS in the OFF-state which suggests the OFF current mechanism to be tunneling through the ML region. (f) Energy-resolved current in the OFF-state. Insets of parts (d) and (f) illustrate the charge difference density of the BL-ML device in the ON and OFF-states where blue (pink) represents depletion (accumulation) of electrons.

structure (see Fig. SI18). The significantly reduced OFF current (> 2.5 orders of magnitude) of the BL-ML device compared to the ML device is identified to be due to: (i) less density of states at the BL-side (being a semiconductor) of the tunneling region in the BL-ML device as opposed to the metallic electrode in the ML device, resulting in significantly suppressed electron transmission, and (ii) bandgap of the BL region blocking almost half of the tunneling energy window in the BL-ML structure (see insets of Fig. SI18). Therefore, the two factors involved in the OFF current transport mechanism are not dependent on the edge-induced states at the BL-ML edge.

The charge difference density (CDD) of the BL-ML device in the ON- and OFF-states is illustrated in the insets of Fig. 4(d,f), which demonstrate electron accumulation (depletion) in the ON (OFF) state. More specifically, it is shown that with ON conditions ($V_{GS} = +0.3$ V) the entire channel is accumulated. However, with OFF conditions ($V_{GS} = -0.6$ V) the gated region of the channel, where energy states exist in the V_{DS} bias window (source chemical potential – drain chemical potential = 0.2 V), is depleted. However, BL-ML edge-induced states below the source chemical potential are occupied and hence are not fully depleted, resulting in a slight accumulation at the BL-ML edge and the transition region adjacent to the edge.

This insight into the underlying physics governing the device performance would be useful for device optimization by engineering the dimensions of the gated region and underlap region at the BL-side (source), taking into account the transition region at the BL-ML interface to further enhance the ON current and hence the device performance.

3. Discussion

The edge-rich nature of TAC-grown polycrystalline $PtSe_2$ films was studied by a combination of microscopy methods including SEM, STEM, AFM and STM. The energy profile of step edges was investigated and the origin of edge-induced states observed by STS mapping were explored through theoretical surface Green's function methods, supported by atomically resolved STEM imaging. Although environmental factors may also influence the properties of the step edges, the correlation between experiment and theory indicates the step edge-induced states are a fundamental and crucial feature for $PtSe_2$, which has to be taken into account for use of such polycrystalline films. Both Pt and Se terminated step edges were found to be present and exhibit distinct properties. Our results reveal that Se-termination of the edges leads to the formation of states at energies near the conduction and valence band edges while Pt-termination of the edges creates energy states throughout the bandgap, making the edge metallic and extending to ~2–2.5 nm from the edge. Furthermore, our fully relativistic DFT calculations reveal large spin splitting of maximum 450 meV and spin magnetic moment of 0.39 μB for the Pt-terminated edge structure indicating its potential for spintronic applications. Due to the strong interlayer interaction and thickness-dependent bandgap in $PtSe_2$, a ML-BL structure can form a lateral monomaterial heterojunction demonstrating straddling type band alignment. The role of the edge-induced energy states and their impact on the carrier transport through the step edge, explored through a concept FET, consisting of the lateral ML-BL heterojunction as the channel. The combined impacts of the suppressed DoS in the BL side and the tunneling distance in the OFF-state, lead to a $>10^{10}$ I_{ON}/I_{OFF} ratio and ~64 mV/dec subthreshold slope. We believe that this study provides insight into the electrical behavior of large-area back-end-of-line compatible grown polycrystalline films and the device concept offers exciting opportunities to further improve the performance of TMD-based electronic devices.

4. Experimental methods

4.1. Synthesis and transfer of $PtSe_2$

Pt films of 5 nm were deposited on SiO_2/Si substrates by argon-ion sputtering (Gatan Precision Etching and Coating System (PECS)). $PtSe_2$ was obtained by annealing the samples at 450 °C for two hours under a 150 sccm H_2/Ar flow, in the presence of an upstream Se metal source heated to approximately 250 °C [31,32]

For conductive measurements the $PtSe_2$ was liberated from the growth substrates by wet etching, as noted in Fig. 1(b). Conductive substrates were prepared by depositing Au/Ti (35 nm/5 nm) onto a SiO_2/Si substrates using a Temescal FC2000 electron-beam evaporation system. The $PtSe_2/SiO_2$/Si samples were floated on a 2 molar NaOH solution. When the substrate had detached from the surface film, the floating films were fished from the solution with a glass slide and refloated in de-ionized water. The films were then lifted out on the prepared conductive substrates, rinsed with deionized water, and dried. For the films with an initial 5 nm Pt thickness, it was possible to transfer without the aid of PMMA, reducing contamination for STM studies. Spin-coated PMMA is required to support thinner films during the transfer process, after transfer and drying the supporting PMMA was dissolved by acetone and the films were washed in isopropyl alcohol.

4.2. Sample characterization

A low-temperature STM from Createc was used for all STM/STS experiments. The experiments were carried out under ultra-high vacuum (UHV) conditions with a base pressure $\sim 3 \times 10^{-11}$ mbar. All the STM images were recorded at 77 K in constant current mode (CCM). The preparation chamber of the STM is fitted with a heating stage for annealing the samples. Electrochemically-etched (001)-oriented single-crystalline tungsten tips in NaOH were cleaned *in situ* with argon-ion bombardment. The bias was applied to the sample with respect to the tip. It was possible to image the surface without heat treatment in vacuum. However, since the sample was wet transferred using an NaOH etching solution which might influence the edge structures, to reduce possible contamination and to improve the quality of the obtained images the sample was subject to a mild annealing, up to 220 °C for 7 hours in UHV, similar to procedures used elsewhere [33,63]. For STS, at each point the spectra were averaged from 15 I(V)-data. The STM tip height was stabilized by the CCM scanning parameters when it was moved across the grid. The CCM scanning parameters used to move between points were V = 0.8 V and I = 100 pA. The corresponding dI/dV maps in this work were obtained by numerical differentiation of plots extracted from the I-V map that was measured by grid spectroscopy.

XPS spectra of the Pt 4f and Se 3d core-levels were measured utilizing a monochromated Omicron MultiProbe XPS system with an aluminum X-ray radiation source (1486.7 eV) and instrumental resolution of 0.6 eV under UHV conditions (5×10^{-11} mbar). After subtraction of a Shirley background, the core-level spectra were fitted with a combination of Gaussian-Lorentzian line shapes using the CasaXPS software.

STEM imaging was performed using a Nion UltraSTEM100 operated at a 60 kV accelerating voltage in near-UHV ($\sim 10^{-9}$ mbar) using a HAADF detector with a collection angle of 80–300 mrad. The convergence semiangle of the electron probe was 30 mrad. The background of HAADF images shown in Fig. 2(a, b) was removed by subtracting a Gaussian blurred (radius 20 px) copy of the image. These HAADF images were further processed using double Gaussian filtering [64]. and Wiener filtering [77]. in order to reduce noise and increase contrast of the images. SEM images were acquired using a Karl Zeiss Supra microscope operating at 3 kV accelerating voltage with a working distance of ~3–4 mm and a 30 μm aperture.

AFM was performed with a Bruker Multimode 8 in PF-TUNA mode using Adama Innovations Super Sharp boron doped conductive diamond coated probes (model: AD-2.8-SS).

Raman spectra were gathered using a WITec Alpha 300 R confocal Raman microscope at 100 × magnification with a 532 nm excitation source and a spectral grating of 1800 lines/mm.

4.3. Density functional theory

The edge structural configurations were obtained and the electronic structure calculations were performed within the framework of Kohn-Sham DFT and surface Green's function (SGF), as implemented in QuantumATK package [78,79]. In the SGF calculations, periodic boundary condition was applied only along the directions parallel to the edge plane. In order to study a realistic single-edge structure similar to an experimental one, as opposed to a conventionally used double-edge in a slab model, a recently developed SGF method has been employed in our calculations. This method allows a semi-infinite structure to be considered enabling charge transfer between the bulk and the edge regions, self-consistently, in a full quantum-mechanical treatment. The norm-conserving pseudopotentials and pseudo-atomic localized basis were used with Perdew-Burke-Ernzerhof (PBE) of generalized gradient approximation (GGA) to describe the exchange correlation energy [80]. OpenMX numerical atomic orbital basis sets s4p3d2 and s4p3d3 were used for Pt and Se, respectively [81]. Geometry optimization was performed using LBFGS (low-memory BFGS) algorithm. Moreover, in the cell optimization the Bravais lattice type was kept constant. Structural optimization was achieved by minimizing the total energy with respect to the atomic positions until the maximum force component became less than 0.01 eV/Å. Monkhorst-Pack scheme [82]. for Brillouin-zone integrations with a density of approximately 10 k-points per angstrom has been considered. An energy cut-off of 120 Ha and energy convergence criterion of 10^{-7} Ha have also been considered. For discretized grid, ~520 k-point per angstrom have been used for the SGF calculations, in the direction normal to the edge plane. We have incorporated van-der-Waals (vdW) interaction for bilayer $PtSe_2$ structures by adding a nonlocal vdW term to the local and the semi-local exchange correlation functionals utilizing Grimme's dispersion correction [83]

To describe the single edge of the $PtSe_2$ monolayer and bilayer, a surface configuration consisting of an electrode and a central region were considered, where the electrode describes the bulk properties of the system and the central region provides the effects of the edge states. Green's function couples the central region Hamiltonian to semi-infinite monolayer or bilayer $PtSe_2$ with periodic boundary condition along x- and y-directions and with open boundary condition along out-of-edge-plane direction (z-direction) - see Fig. 2(c, d). Self-energy matrix describes the semi-infinite electrode which is created by a recursive method [79]. For type A configuration, 110 (300) Å was considered for ML (BL), and for type B, 200 (300) Å was considered for ML (BL) as the length of the central region to converge the electrostatic potential with respect to the periodic potential of the electrode (see Fig. SI19).

To obtain the band alignment at the BL-ML heterojunction, non-equilibrium quantum transport calculations were performed based on first-principles calculations. DFT together with the non-equilibrium Green's functions (NEGF) technique (DFT+NEGF) was utilized to represent realistic open systems to determine the coherent transport properties of the system fully self-consistently [84]. For discretized grid, ~520 k-point per angstrom have been used for the NEGF calculations, in the channel axis, i.e., z-direction.

To investigate the effects of SOC on the edge states, the electronic structure calculations were performed with and without the consideration of SOC using fully relativistic pseudo potentials.

4.4. FET model

The simulation cell of the heterojunction in the BL-ML FET structure has a cross sectional area of 0.376 × 4 nm^2 parallel to the junction, i.e., (x,y) plane, where the 0.376 nm is the repeat unit in the plane of the film (x-direction) and the 4 nm is the repeat unit normal to the film (y-direction), considering the periodic boundary condition in the (x,y) plane. The length normal to the junction (z-direction) is 29.56 nm with 16.45 nm bilayer and 13.11 nm monolayer $PtSe_2$, including the ~2 nm source and drain regions under the Al contacts. Al metal was considered as the source and drain electrodes and the gate-oxide was described through electrostatic coupling of a continuum with hafnium oxide dielectric constant of $\epsilon_{HfO_2} = 25$ and thickness of 1 nm [85,86]. The gate length was 15 nm for the BL-ML device, centered at the step edge, and 7.5 nm for the ML device. Since the simulations and experiments have shown that the edge-induced states propagate further into the thicker side of the BL-ML junction, a longer BL region was considered to allow all possible effects to be accommodated. This configuration resulted in asymmetric underlap regions in the BL-ML junction channel, i.e., the underlap region is ~6 nm and ~2.7 nm at the BL (source) and ML (drain) sides of the BL-ML channel respectively, while it is ~2.7 nm in both source and drain sides of the ML channel.

To capture the performance of the back-gated FETs, the DFT+NEGF approach was employed [87,88]. Semi-infinite electrodes, which consist of the Al contact and the underlying $PtSe_2$ region, were described by the self-energies defined in the DFT+NEGF framework. OpenMX numerical atomic orbital basis sets s4p4d2 were used for Al atoms. In the device transfer characteristics calculation, the electrode conditions were achieved by holding the source and drain regions at thermal equilibrium described by the Fermi-Dirac distributions at T = 300 K, and by considering chemical potential difference $\mu_{DS} = qV_{DS}$ for the drain-source bias. Electron transmission under each bias condition (T(E, V_{DS},V_{GS})) was calculated self-consistently in the DFT+NEGF approach. Upon obtaining the electron transmission, the drain-source current (I_{DS}) was calculated using the Landauer–Büttiker formula [89]:

$$I_{DS} = \int i(E)dE,$$

$$i(E) = \frac{e}{h}T(E, V_{DS}, V_{GS})[f_S(E) - f_D(E)]$$

where E, e, and h are energy, electron charge, and Planck's constant, respectively. T is transmission, and $f_S(E)$ and $f_D(E)$ are the Fermi-Dirac distribution functions at the source and drain electrodes, respectively.

Subthreshold slope (SS), which is defined as the inverse of the derivative of log of drain current with respect to the gate voltage, i.e., $SS = \left(\frac{d(\log_{10}(I_{DS}))}{dV_{GS}}\right)^{-1}$, is a measure of the electrostatic control of gate (V_{GS}) over the drain-source current (I_{DS}) in a field effect transistor.

Author contributions

The manuscript was written through contributions of all authors. L. A. and F.G. conducted the theoretical calculations and atomic-scale simulations. N.M. and C.Ó. synthesized $PtSe_2$ films and performed Raman, SEM, AFM characterization and analysis. K.Z. performed STM and STS, and analysis. A.Z. performed XPS and helped with characterization and analysis. K.E. and J.K. performed TEM and analysis. K.Z., L. A. N.M. C.Ó. and F.G. conceived and designed the experiments and wrote the manuscript. I.V.S, P.K.H. and G.S.D. helped with the planning of the experiments, interpretation of the results, and supervision of the project. All authors discussed the results and reviewed the manuscript.

CRediT authorship contribution statement

Kuanysh Zhussupbekov: Methodology, Formal analysis, Investigation, Data curation, Visualization, Writing – original draft, Writing – review & editing, Funding acquisition. **Lida Ansari:** Methodology, Formal analysis, Investigation, Data curation, Visualization, Writing – original draft, Writing – review & editing. **Kenan Elibol:** Investigation, Data curation, Visualization, Writing – review & editing. **Ainur Zhussupbekova:** Investigation, Data curation, Visualization, Writing –

review & editing. **Jani Kotakoski:** Investigation, Data curation, Visualization, Writing – review & editing. **Igor V. Shvets:** Conceptualization, Resources, Supervision, Writing – review & editing, Funding acquisition. **Georg S. Duesberg:** Conceptualization, Resources, Supervision, Writing – review & editing, Funding acquisition. **Paul K. Hurley:** Conceptualization, Resources, Supervision, Writing – review & editing, Funding acquisition. **Niall McEvoy:** Methodology, Investigation, Data curation, Visualization, Resources, Writing – original draft, Writing – review & editing. **Cormac Ó Coileáin:** Conceptualization, Methodology, Investigation, Data curation, Visualization, Writing – original draft, Writing – review & editing. **Farzan Gity:** Conceptualization, Methodology, Formal analysis, Investigation, Data curation, Visualization, Writing – original draft, Writing – review & editing.

Declaration of Competing Interest

The authors declare that they have no known competing financial interests or personal relationships that could have appeared to influence the work reported in this paper

Data availability

Data will be made available on request.

Acknowledgments

I.V.S., K.Z. and A.Z. acknowledge the support of Irish Research Council (IRC) through (IRCLA/2019/171). K.Z would like acknowledge support from Ministry of Science and Higher Education of the Republic of Kazakhstan (No AP19174589). K.Z. and A.Z. would also like to acknowledge funding from IRC through GOIPD/2022/774 and GOIPD/2022/443 awards. C.Ó., G.S.D., N.M., P.H and F.G. acknowledge support from SFI through 15/SIRG/3329, 12/RC/2278_P2 and SFI PI_15/IA/3131. C.Ó. and G.S.D acknowledge the German Ministry of Education and Research (BMBF) under the project NobleNEMS [16ES1121], the European Union under the project Queformal [829035] and NextGenerationEU for dtec.bw for project VITAL-SENSE. SFI/HEA Irish Center for High-End Computing (ICHEC) is acknowledged for the provision of computational facilities and support. L.A. would also like to acknowledge funding from IRC through award GOIPD/2018/653.

Supplementary materials

Supplementary material associated with this article can be found, in the online version, at doi:10.1016/j.apmt.2023.101926.

References

[1] Q.H. Wang, K. Kalantar-Zadeh, A. Kis, J.N. Coleman, M.S. Strano, Electronics and optoelectronics of two-dimensional transition metal dichalcogenides, Nat. Nanotechnol. 7 (2012) 699–712, https://doi.org/10.1038/nnano.2012.193.
[2] J.B. Mc Manus, et al., Low-temperature synthesis and electrocatalytic application of large-area PtTe2 thin films, Nanotechnology 31 (2020), 375601, https://doi.org/10.1088/1361-6528/ab9973.
[3] W.J. Zhu, T. Low, H. Wang, P.D. Ye, X.F. Duan, Nanoscale electronic devices based on transition metal dichalcogenides, 2D Mater. 6 (2019) 17, https://doi.org/10.1088/2053-1583/ab1ed9.
[4] G.Z. Wang, Z.Z. Wang, N. McEvoy, P. Fan, W.J. Blau, Layered PtSe2 for sensing, photonic, and (Opto-)electronic applications, Adv. Mater. 33 (2021) 23, https://doi.org/10.1002/adma.202004070.
[5] L.J. Pi, et al., Recent progress on 2D noble-transition-metal dichalcogenides, Adv. Funct. Mater. 29 (2019) 22, https://doi.org/10.1002/adfm.201904932.
[6] E. Chen, W. Xu, J. Chen, J.H Warner, 2D layered noble metal dichalcogenides (Pt, Pd, Se, S) for electronics and energy applications, Mater. Today Adv. 7 (2020) 35, https://doi.org/10.1016/j.mtadv.2020.100076.
[7] D. Jariwala, V.K. Sangwan, L.J. Lauhon, T.J. Marks, M.C. Hersam, Emerging device applications for semiconducting two-dimensional transition metal dichalcogenides, ACS Nano 8 (2014) 1102–1120, https://doi.org/10.1021/nn500064s.
[8] S.H. Lin, et al., Tunable active edge sites in PtSe2 films towards hydrogen evolution reaction, Nano Energy 42 (2017) 26–33, https://doi.org/10.1016/j.nanoen.2017.10.038.
[9] Y.H. Kim, et al., Ultrasensitive reversible oxygen sensing by using liquid-exfoliated MoS2 nanoparticles, J. Mater. Chem. A 4 (2016) 6070–6076, https://doi.org/10.1039/c6ta01277a.
[10] A. Avsar, et al., Defect induced, layer-modulated magnetism in ultrathin metallic PtSe2, Nat. Nanotechnol. 14 (2019), https://doi.org/10.1038/s41565-019-0467-1, 674-+.
[11] J. Ge, et al., Magnetic moments induced by atomic vacancies in transition metal dichalcogenide flakes, Adv. Mater. 33 (2021) 7, https://doi.org/10.1002/adma.202005465.
[12] F. Schedin, et al., Detection of individual gas molecules adsorbed on graphene, Nat. Mater. 6 (2007) 652–655, https://doi.org/10.1038/nmat1967.
[13] J. Sun, M. Muruganathan, H. Mizuta, Room temperature detection of individual molecular physisorption using suspended bilayer graphene, Sci. Adv. 2 (2016) 7, https://doi.org/10.1126/sciadv.1501518.
[14] H.S. Zheng, et al., Visualization of point defects in ultrathin layered 1T-PtSe2, 2D Mater. 6 (2019) 9, https://doi.org/10.1088/2053-1583/ab3beb.
[15] K. Zhussupbekov, et al., Imaging and identification of point defects in PtTe2, npj 2D Mater. Appl. 5 (2021) 10, https://doi.org/10.1038/s41699-020-00196-8.
[16] S. Barja, et al., Identifying substitutional oxygen as a prolific point defect in monolayer transition metal dichalcogenides, Nat. Commun. 10 (2019) 8, https://doi.org/10.1038/s41467-019-11342-2.
[17] B. Schuler, et al., Large spin-orbit splitting of deep in-gap defect states of engineered sulfur vacancies in monolayer WS2, Phys. Rev. Lett 123 (2019) 7, https://doi.org/10.1103/PhysRevLett.123.076801.
[18] K. Nakada, M. Fujita, G. Dresselhaus, M.S. Dresselhaus, Edge state in graphene ribbons: nanometer size effect and edge shape dependence, Phys. Rev. B 54 (1996) 17954–17961, https://doi.org/10.1103/PhysRevB.54.17954.
[19] X. Wu, et al., Shallowing interfacial carrier trap in transition metal dichalcogenide heterostructures with interlayer hybridization, Nano Res. 14 (2021) 1390–1396, https://doi.org/10.1007/s12274-020-3188-8.
[20] F. Lupke, et al., Proximity-induced superconducting gap in the quantum spin Hall edge state of monolayer WTe2, Nat. Phys. 16 (2020), https://doi.org/10.1038/s41567-020-0816-x, 526-+.
[21] L. Peng, et al., Observation of topological states residing at step edges of WTe2, Nat. Commun. 8 (2017) 7, https://doi.org/10.1038/s41467-017-00745-8.
[22] S. Liu, H.Y. Zhu, Z.R. Liu, G.H. Zhou, Symmetrical metallic and magnetic edge states of nanoribbon from semiconductive monolayer PtS2, Phys. Lett. A 382 (2018) 776–780, https://doi.org/10.1016/j.physleta.2018.01.021.
[23] C.J. Zhang, et al., Additive-free MXene inks and direct printing of micro-supercapacitors, Nat. Commun. 10 (2019) 1795, https://doi.org/10.1038/s41467-019-09398-1.
[24] D. McManus, et al., Water-based and biocompatible 2D crystal inks for all-inkjet-printed heterostructures, Nat. Nanotechnol. 12 (2017) 343–350, https://doi.org/10.1038/nnano.2016.281.
[25] A. Banerjee, H. Bhunia, A.J. Pal, 2D analogue of band-bending in metal-semiconductor junctions: interior to edge-states of single-layered transition metal dichalcogenides, J. Phys. D Appl. Phys 54 (2021) 7, https://doi.org/10.1088/1361-6463/abc9e7.
[26] L. Klopotowski, et al., Revealing the nature of excitons in liquid exfoliated monolayer tungsten disulphide, Nanotechnology 27 (2016) 9, https://doi.org/10.1088/0957-4484/27/42/425701.
[27] C. Yim, et al., Electrical devices from top-down structured platinum diselenide films, npj 2D Mater. Appl. 2 (2018) 7, https://doi.org/10.1038/s41699-018-0051-9.
[28] B.M. Szydlowska, et al., Spectroscopic thickness and quality metrics for PtSe(2) layers produced by top-down and bottom-up techniques, 2D Mater. 7 (2020) 12, https://doi.org/10.1088/2053-1583/aba9a0.
[29] R. Kempt, A. Kuc, T. Heine, Two-dimensional noble-metal chalcogenides and phosphochalcogenides, Angew. Chem. Int. Ed. 59 (2020) 9242–9254, https://doi.org/10.1002/anie.201914886.
[30] Y.L. Wang, et al., Monolayer PtSe2, a new semiconducting transition-metal-dichalcogenide, epitaxially grown by direct selenization of Pt, Nano Lett. 15 (2015) 4013–4018, https://doi.org/10.1021/acs.nanolett.5b00964.
[31] C. Yim, et al., High-performance hybrid electronic devices from layered PtSe2 films grown at low temperature, ACS Nano 10 (2016) 9550–9558, https://doi.org/10.1021/acsnano.6b04898.
[32] L. Ansari, et al., Quantum confinement-induced semimetal-to-semiconductor evolution in large-area ultra-thin PtSe2 films grown at 400 degrees C, npj 2D Mater. Appl. 3 (2019) 8, https://doi.org/10.1038/s41699-019-0116-4.
[33] J. Li, et al., Layer-dependent band gaps of platinum dichalcogenides, ACS Nano 15 (2021) 13249–13259, https://doi.org/10.1021/acsnano.1c02971.
[34] P. Miro, M. Ghorbani-Asl, T. Heine, Two dimensional materials beyond MoS2: noble-transition-metal dichalcogenides, Angew. Chem. Int. Ed. 53 (2014) 3015–3018, https://doi.org/10.1002/anie.201309280.
[35] P.F. Li, L. Li, X.C. Zeng, Tuning the electronic properties of monolayer and bilayer PtSe2 via strain engineering, J. Mater. Chem. C 4 (2016) 3106–3112, https://doi.org/10.1039/c6tc00130k.
[36] S.S. Han, et al., Horizontal-to-vertical transition of 2D layer orientation in low-temperature chemical vapor deposition-grown PtSe2 and its influences on electrical properties and device applications, ACS Appl. Mater. Interfaces 11 (2019) 13598–13607, https://doi.org/10.1021/acsami.9b01078.
[37] L.K. Li, et al., Black phosphorus field-effect transistors, Nat. Nanotechnol. 9 (2014) 372–377, https://doi.org/10.1038/nnano.2014.35.

[38] W.X. Zhang, Z.S. Huang, W.L. Zhang, Y.R. Li, Two-dimensional semiconductors with possible high room temperature mobility, Nano Res. 7 (2014) 1731–1737, https://doi.org/10.1007/s12274-014-0532-x.
[39] W. Yao, et al., Direct observation of spin-layer locking by local Rashba effect in monolayer semiconducting PtSe2 film, Nat. Commun. 8 (2017) 6, https://doi.org/10.1038/ncomms14216.
[40] M. Meng, et al., Ferromagnetism regulated by edged cutting and optical identification in monolayer PtSe2 nanoribbons, J. Phys. D Appl. Phys 51 (2018) 8, https://doi.org/10.1088/1361-6463/aabf30.
[41] S.D. Guo, Biaxial strain tuned thermoelectric properties in monolayer PtSe2, J. Mater. Chem. C 4 (2016) 9366–9374, https://doi.org/10.1039/c6tc03074b.
[42] T.-Y. Su, et al., Thermally strain-induced band gap opening on platinum diselenide-layered films: a promising two-dimensional material with excellent thermoelectric performance, Chem. Mater. 33 (2021) 3490–3498, https://doi.org/10.1021/acs.chemmater.0c04351.
[43] C.S. Boland, et al., PtSe2 grown directly on polymer foil for use as a robust piezoresistive sensor, 2D Mater. 6 (2019) 8, https://doi.org/10.1088/2053-1583/ab33a1.
[44] E. Okogbue, et al., Multifunctional two-dimensional PtSe2-layer kirigami conductors with 2000% stretchability and metallic-to-semiconducting tunability, Nano Lett. 19 (2019) 7598–7607, https://doi.org/10.1021/acs.nanolett.9b01726.
[45] F. Urban, F. Gity, P.K. Hurley, N. McEvoy, A. Di Bartolomeo, Isotropic conduction and negative photoconduction in ultrathin PtSe2 films, Appl. Phys. Lett 117 (2020) 6, https://doi.org/10.1063/5.0021009.
[46] A. Ciarrocchi, A. Avsar, D. Ovchinnikov, A. Kis, Thickness-modulated metal-to-semiconductor transformation in a transition metal dichalcogenide, Nat. Commun. 9 (2018) 6, https://doi.org/10.1038/s41467-018-03436-0.
[47] C. Yim, et al., Wide spectral photoresponse of layered platinum diselenide-based photodiodes, Nano Lett. 18 (2018) 1794–1800, https://doi.org/10.1021/acs.nanolett.7b05000.
[48] L.H. Zeng, et al., Ultrafast and sensitive photodetector based on a PtSe2/silicon nanowire array heterojunction with a multiband spectral response from 200 to 1550nm, NPG Asia Mater. 10 (2018) 352–362, https://doi.org/10.1038/s41427-018-0035-4.
[49] D.K. Hu, et al., Unveiling the layer-dependent catalytic activity of PtSe2 atomic crystals for the hydrogen evolution reaction, Angew. Chem. Int. Ed. 58 (2019) 6977–6981, https://doi.org/10.1002/anie.201901612.
[50] Y. Chang, P. Zhai, J. Hou, J. Zhao, J. Gao, Excellent HER and OER catalyzing performance of Se-vacancies in defects-engineered PtSe2: from simulation to experiment, Adv. Energy Mater. (2021), 2102359, https://doi.org/10.1002/aenm.202102359 n/a.
[51] A. Avsar, et al., Probing magnetism in atomically thin semiconducting PtSe2, Nat. Commun 11 (2020) 7, https://doi.org/10.1038/s41467-020-18521-6.
[52] S. Lukas, et al., Correlating nanocrystalline structure with electronic properties in 2D platinum diselenide, Adv. Funct. Mater 31 (2021) 11, https://doi.org/10.1002/adfm.202102929.
[53] P.V. Sarma, et al., Electrocatalysis on edge-rich spiral WS2 for hydrogen evolution, ACS Nano 13 (2019) 10448–10455, https://doi.org/10.1021/acsnano.9b04250.
[54] T. Das, et al., Doping-free all PtSe2 transistor via thickness-modulated phase transition, ACS Appl. Mater. Interfaces 13 (2021) 1861–1871, https://doi.org/10.1021/acsami.0c17810.
[55] E. Yang, J.E. Seo, D. Seo, J. Chang, Intrinsic limit of contact resistance in the lateral heterostructure of metallic and semiconducting PtSe2, Nanoscale 12 (2020) 14636–14641, https://doi.org/10.1039/d0nr03001e.
[56] Y.J. Yang, S.K. Jang, H.J. Choi, J. Xu, S. Lee, Homogeneous platinum diselenide metal/semiconductor coplanar structure fabricated by selective thickness control, Nanoscale 11 (2019) 21068–21073, https://doi.org/10.1039/c9nr07995e.
[57] M. Ghorbani-Asl, A. Kuc, P. Miro, T. Heine, A single-material logical junction based on 2D crystal PdS2, Adv. Mater. 28 (2016) 853–856, https://doi.org/10.1002/adma.201504274.
[58] M. O'Brien, et al., Raman characterization of platinum diselenide thin films, 2D Mater. 3 (2016) 7, https://doi.org/10.1088/2053-1583/3/2/021004.
[59] G.Z. Wang, et al., Ultrafast carrier dynamics and bandgap renormalization in layered PtSe2, Small 15 (2019) 9, https://doi.org/10.1002/smll.201902728.
[60] X. Lin, et al., Intrinsically patterned two-dimensional materials for selective adsorption of molecules and nanoclusters, Nat. Mater. 16 (2017), https://doi.org/10.1038/Nmat4915, 717-+.
[61] Z.L. Liu, et al., Using graphene to suppress the selenization of Pt for controllable fabrication of monolayer PtSe2, Nano Res. 13 (2020) 3212–3216, https://doi.org/10.1007/s12274-020-2989-0.
[62] Y.F. Tong, et al., Phase transition and thermal stability of epitaxial PtSe(2) nanolayer on Pt(111), RSC Adv. 10 (2020) 30934–30943, https://doi.org/10.1039/d0ra04346j.
[63] J. Li, et al., Edge and point-defect induced electronic and magnetic properties in monolayer PtSe2, Adv. Funct. Mater. 32 (2022), 2110428, https://doi.org/10.1002/adfm.202110428.
[64] O.L. Krivanek, et al., Atom-by-atom structural and chemical analysis by annular dark-field electron microscopy, Nature 464 (2010) 571–574, https://doi.org/10.1038/nature08879.
[65] D. Li, F. Ding, Environment-dependent edge reconstruction of transition metal dichalcogenides: a global search, Mater. Today Adv 8 (2020) 8, https://doi.org/10.1016/j.mtadv.2020.100079.
[66] K. Elibol, et al., Atomic structure of intrinsic and electron-irradiation-induced defects in MoTe2, Chem. Mater. 30 (2018) 1230–1238, https://doi.org/10.1021/acs.chemmater.7b03760.
[67] G.H. Ryu, J. Chen, Y. Wen, J.H. Warner, *In-situ* atomic-scale dynamics of thermally driven phase transition of 2D few-layered 1T PtSe2 into ultrathin 2D nonlayered PtSe crystals, Chem. Mater. 31 (2019) 9895–9903, https://doi.org/10.1021/acs.chemmater.9b04274.
[68] D. Wu, et al., Uncovering edge states and electrical inhomogeneity in MoS2 field-effect transistors, Proc. Natl. Acad. Sci. U. S. A 113 (2016) 8583–8588, https://doi.org/10.1073/pnas.1605982113.
[69] S. Bhowmick, V.B. Shenoy, Edge state magnetism of single layer graphene nanostructures, J. Chem. Phys 128 (2008) 7, https://doi.org/10.1063/1.2943678.
[70] Y. Nakanishi, et al., Large edge magnetism in oxidized few-layer black phosphorus nanomeshes, Nano Res. 10 (2017) 718–728, https://doi.org/10.1007/s12274-016-1355-8.
[71] L. Jelver, D. Stradi, K. Stokbro, T. Olsen, K.W. Jacobsen, Spontaneous breaking of time-reversal symmetry at the edges of 1T′ monolayer transition metal dichalcogenides, Phys. Rev. B 99 (2019), 155420, https://doi.org/10.1103/PhysRevB.99.155420.
[72] S. Liu, H. Zhu, Z. Liu, G. Zhou, Symmetrical metallic and magnetic edge states of nanoribbon from semiconductive monolayer PtS2, Phys. Lett. A 382 (2018) 776–780, https://doi.org/10.1016/j.physleta.2018.01.021.
[73] K. Zhussupbekov, et al., Oxidation of Nb(110): atomic structure of the NbO layer and its influence on further oxidation, Sci. Rep. 10 (2020) 9, https://doi.org/10.1038/s41598-020-60508-2.
[74] K. Zhussupbekov, et al., Electronic and structural characterisation of polycrystalline platinum disulfide thin films, RSC Adv. 10 (2020) 42001–42007, https://doi.org/10.1039/d0ra07405e.
[75] C.D. Zhang, et al., Visualizing band offsets and edge states in bilayer-monolayer transition metal dichalcogenides lateral heterojunction, Nat. Commun. 7 (2016) 6, https://doi.org/10.1038/ncomms10349.
[76] K. Zhussupbekov, et al., Surface modification and subsequent fermi density enhancement of Bi(111), J. Phys. Chem. C 125 (2021) 5549–5558, https://doi.org/10.1021/acs.jpcc.0c07345.
[77] V. Grillo, F. Rossi, STEM_CELL: a software tool for electron microscopy. Part 2 analysis of crystalline materials, Ultramicroscopy 125 (2013) 112–129, https://doi.org/10.1016/j.ultramic.2012.10.009.
[78] S. Smidstrup, et al., QuantumATK: an integrated platform of electronic and atomic-scale modelling tools, J. Phys. Condes. Matter 32 (2020) 36, https://doi.org/10.1088/1361-648X/ab4007.
[79] S. Smidstrup, et al., First-principles Green's-function method for surface calculations: A pseudopotential localized basis set approach, Phys. Rev. B 96 (2017) 17, https://doi.org/10.1103/PhysRevB.96.195309.
[80] J.P. Perdew, K. Burke, M. Ernzerhof, Generalized gradient approximation made simple, Phys. Rev. Lett. 77 (1996) 3865–3868, https://doi.org/10.1103/PhysRevLett.77.3865.
[81] T. Ozaki, Variationally optimized atomic orbitals for large-scale electronic structures, Phys. Rev. B 67 (2003) 5, https://doi.org/10.1103/PhysRevB.67.155108.
[82] H.J. Monkhorst, J.D. Pack, Special points for Brillouin-zone integrations, Phys. Rev. B 13 (1976) 5188–5192, https://doi.org/10.1103/PhysRevB.13.5188.
[83] S. Grimme, Semiempirical GGA-type density functional constructed with a long-range dispersion correction, J. Comput. Chem 27 (2006) 1787–1799, https://doi.org/10.1002/jcc.20495.
[84] S.H. Ke, H.U. Baranger, W.T. Yang, Electron transport through molecules: self-consistent and non-self-consistent approaches, Phys. Rev. B 70 (2004) 12, https://doi.org/10.1103/PhysRevB.70.085410.
[85] L. Ansari, G. Fagas, J.P. Colinge, J.C. Greer, A proposed confinement modulated gap nanowire transistor based on a metal (Tin), Nano Lett. 12 (2012) 2222–2227, https://doi.org/10.1021/nl2040817.
[86] L. Ansari, G. Fagas, F. Gity, J.C. Greer, A sub k(B)T/q semimetal nanowire field effect transistor, Appl. Phys. Lett 109 (2016) 5, https://doi.org/10.1063/1.4960709.
[87] M. Brandbyge, J.L. Mozos, P. Ordejon, J. Taylor, K. Stokbro, Density-functional method for nonequilibrium electron transport, Phys. Rev. B 65 (2002) 17, https://doi.org/10.1103/PhysRevB.65.165401.
[88] D. Stradi, U. Martinez, A. Blom, M. Brandbyge, K. Stokbro, General atomistic approach for modeling metal-semiconductor interfaces using density functional theory and nonequilibrium Green's function, Phys. Rev. B 93 (2016) 11, https://doi.org/10.1103/PhysRevB.93.155302.
[89] S. Datta, Electronic Transport in Mesoscopic Systems, Cambridge University Press, 1995.